Altered functional properties of a *TRPM2* variant in Guamanian ALS and PD

Meredith C. Hermosura[a,1], Aaron M. Cui[a], Ramon Christopher V. Go[a], Bennett Davenport[b], Cory M. Shetler[a], Justin W. Heizer[b], Carsten Schmitz[c], Gabor Mocz[a], Ralph M. Garruto[d], and Anne-Laure Perraud[b]

[a]Pacific Biosciences Research Center, University of Hawaii at Manoa, Honolulu, HI 96822; [b]National Jewish Medical and Research Center, Denver, CO 80206; [c]University of Colorado Health Sciences Center, Denver, CO 80206; and [d]Laboratory of Biomedical Anthropology and Neurosciences, State University of New York at Binghamton, Binghamton, NY 13902

Edited by David E. Clapham, Harvard Medical School, Boston, MA, and approved September 30, 2008 (received for review August 26, 2008)

Two related neurodegenerative disorders, Western Pacific amyotrophic lateral sclerosis (ALS) and parkinsonism–dementia (PD), originally occurred at a high incidence on Guam, in the Kii peninsula of Japan, and in southern West New Guinea more than 50 years ago. These three foci shared a unique mineral environment characterized by the presence of severely low levels of Ca^{2+} and Mg^{2+}, coupled with high levels of bioavailable transition metals in the soil and drinking water. Epidemiological studies suggest that genetic factors also contribute to the etiology of these disorders. Here, we report that a variant of the transient receptor potential melastatin 2 (*TRPM2*) gene may confer susceptibility to these diseases. *TRPM2* encodes a calcium-permeable cation channel highly expressed in the brain that has been implicated in mediating cell death induced by oxidants. We found a heterozygous variant of *TRPM2* in a subset of Guamanian ALS (ALS-G) and PD (PD-G) cases. This variant, $TRPM2^{P1018L}$, produces a missense change in the channel protein whereby proline 1018 (Pro^{1018}) is replaced by leucine (Leu^{1018}). Functional studies revealed that, unlike WT TRPM2, P1018L channels inactivate. Our results suggest that the ability of TRPM2 to maintain sustained ion influx is a physiologically important function and that its disruption may, under certain conditions, contribute to disease states.

calcium | neurodegeneration | oxidative stress | channelopathy | gene environment

Complex diseases such as cardiovascular and neurodegenerative disorders are believed to be caused by a multitude of factors, including environmental triggers interacting with genetic susceptibility genes. Among neurodegenerative disorders, Western Pacific amyotrophic lateral sclerosis (ALS) and parkinsonism–dementia (PD) are ideal for studying the relative contributions of genes and environment in disease etiology because they occur in geographically separate foci among three genetically different, homogenous groups of people (1). Intensive research conducted over the years led to the identification of two candidate environmental factors: (*i*) severely low levels of Ca^{2+} and Mg^{2+} in the soil and drinking water (2); and (*ii*) the putative neurotoxin β-methylamino-L-alanine (L-BMAA), derived from the cycad plant, a traditional food source in Guam (3). These findings led to the hypothesis that prolonged exposure to such an environment could be involved in the pathogenesis of Western Pacific ALS and PD (2). Supporting this hypothesis are observations that afflicted individuals exhibit altered Ca^{2+} metabolism, and experimental reports of neuronal damage in experimental models of animals fed diets that mimic the mineral composition in the disease foci environment (4, 5). However, the molecular mechanisms underlying these observations are not known. To address this problem, we sought to identify candidate susceptibility genes whose functions might be affected by these environmental conditions.

We identified two ion channel genes, *TRPM7* and *TRPM2,* as candidates and hypothesized that variants of these genes may produce channels with very slight functional alterations such that the detrimental effect becomes evident only after prolonged exposure to a conducive environment (6). We recently reported our studies on the heterozygous *TRPM7* variant, $TRPM7^{T1482I}$ (7). We have now extended this genotyping analysis to *TRPM2*. TRPM2 channels are highly abundant in immune cells, in insulin-secreting cells, and in the brain, where they are found in microglia and neuronal cells (8–11). TRPM2 belongs to the transient receptor potential (TRP) superfamily, a group of cation channels that are expressed in virtually all tissue and cell types and are involved in various cellular functions, in the most part related to Ca^{2+} signaling. The important role of TRP channels in cell physiology is underscored by the increasing number of reports implicating these proteins in the pathogenesis of many diseases (reviewed in ref. 12). There are 28 mammalian TRP channels, grouped into seven subfamilies, one of which is TRP melastatin (TRPM), so named because the founding member, TRPM1, was first described in connection with metastatic melanomas (12, 13). All eight TRPM family members have been linked to disease, either by functional studies in mouse models or by genetic evidence (7, 12). Like all TRP subunits, the TRPM protein consists of six transmembrane segments and cytosolic N- and C-terminal tails (Fig. 1*A*). It is believed that four monomers form a functional channel and the loop between segment 5 (S5) and segment 6 (S6) forms the channel pore. TRPM2, TRPM6, and TRPM7 share a feature unique among known channels, by having a functional enzyme moiety in the C-terminal domain. In TRPM2, this is a type of Nudix hydrolase (NUDT9-H in Fig. 1*A*) that can bind to and hydrolyze ADP-ribose (ADPR), although not as effectively as other known Nudix ADPR-hydrolases (14). Binding of ADPR to NUDT9-H activates the channel, allowing the passage of cations down their electrochemical gradient. Because TRPM2 is a plasma membrane channel, Ca^{2+} and Na^{+} will flow into the cell when TRPM2 opens. ADPR is the most potent physiological activator of TRPM2, but other less potent activators have been proposed (9, 15–17). These include nicotinamide adenine dinucleotide, oxidants such as H_2O_2, and cyclic ADPR. Nicotinamide adenine dinucleotide and H_2O_2 increase intracellular levels of ADPR and could thus gate TRPM2 indirectly (18).

TRPM2 has been implicated in cell death induced by oxidants (11, 16). The presence of low Mg^{2+} and high transition metals in the Western Pacific ALS and PD foci create conditions of increased oxidative stress (6). As a channel with high expression profile in microglia and neuronal cells that could sense and respond to oxidative stress, *TRPM2* is an attractive candidate susceptibility gene for these disorders. Here, we report our studies on $TRPM2^{P1018L}$, a heterozygous variant of *TRPM2* that we identified

Author contributions: M.C.H. and A.-L.P. designed research; M.C.H., A.M.C., R.C.V.G., B.D., C.M.S., J.W.H., C.S., and G.M. performed research; R.M.G. contributed new reagents/analytic tools; M.C.H. and A.-L.P. analyzed data; and M.C.H. wrote the paper.

The authors declare no conflict of interest.

This article is a PNAS Direct Submission.

[1]To whom correspondence should be addressed. E-mail: meredith@pbrc.hawaii.edu.

This article contains supporting information online at www.pnas.org/cgi/content/full/0808218105/DCSupplemental.

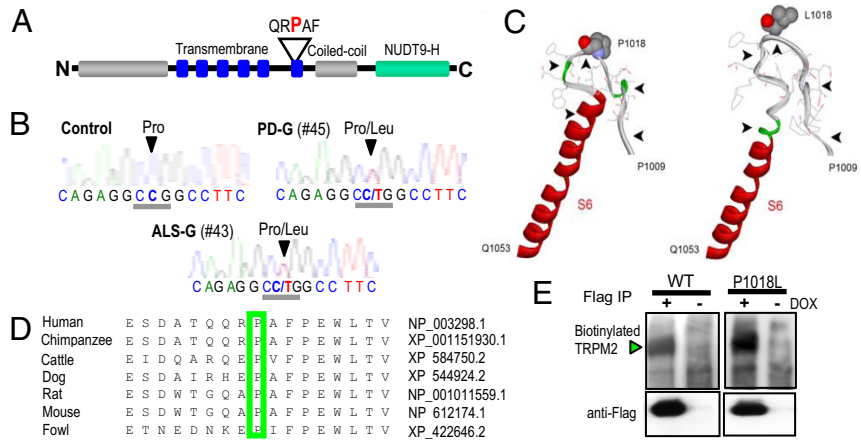

Fig. 1. Genetic and molecular properties of *TRPM2* and *TRPM2*^{P1018L}. (*A*) Schematic diagram of TRPM2 showing the approximate location of Pro^{1018}. (*B*) Representative chromatograms of control, ALS-G, and PD-G sequences. A C-to-T transition converts Pro to Leu (arrowhead). (*C*) Putative 3D model for TRPM2^{WT} and TRPM2^{P1018L}. Only the mutated capping loop at the N terminus of S6 is shown (residues 1009–1053). The colored segments of the backbone structure (solid ribbons) mark the location of α-helix (red), turn (green), and coil (white). The side chains of Pro^{1018} and Leu^{1018} are shown in space-fill form. A few selected side chains (1009–1024) are also shown as lines. Arrows indicate the position of the most affected backbone sections. Notice the larger loop size and local variations in the structure of the loop/turn-helix motif in the Leu^{1018} model. (*D*) Pro^{1018} is evolutionary conserved (boxed). The protein sequences are designated by their National Center for Biotechnology Information accession numbers. (*E*) Surface biotinylation assays of expressed WT and P1018L TRPM2 show that surface expression is not reduced in the mutant.

in a subset of cases of Guamanian ALS (ALS-G) and Guamanian PD (PD-G). In this variant, a missense mutation replaces Pro^{1018} with Leu^{1018}. Our functional studies show that P1018L channels inactivate and are unable to maintain sustained ion flow.

Results

The *TRPM2*^{P1018L} Variant in ALS-G and PD-G. We sequenced genomic DNA extracted from the same set of frozen brain specimens used in the TRPM7 study (7). These pathologically confirmed samples were collected over the years as part of a National Institute of Neurological Disorders and Stroke case ascertainment program for ALS-G and PD-G. They were from men and women of Chamorro heritage (the indigenous people of Guam), and include specimens from age-matched controls. Representative sequence chromatograms are shown in Fig. 1*B* [see supporting information (SI) Fig. S1 for more]. The *TRPM2*^{P1018L} variant was found in four of 13 ALS-G and two of 9 PD-G cases. It was also detected in three of the 22 control samples. However, these three "control" specimens represent two cases of heart failure and one case of tumor, diseases that may have an oxidative stress-related etiology. All samples that were positive for the variant were heterozygous. *TRPM2*^{P1018L} appears to be a rare variant. As of this writing, it has not been described in the publicly accessible SNP databases (http://www.ncbi.nlm.nih.gov/projects/SNP/ or http://www.ensembl.org). This is not unprecedented. The P112Q missense mutation in the related channel, TRPC6, described in connection with familial focal segmental glomerulosclerosis is also a rare genetic variant that is not found in public SNP databases (19).

Computer Modeling Predicts Leu^{1018} Relaxes Structural Constraints. Pro^{1018} is located at the C-terminal end of the pore region, just a few residues upstream of the predicted S6 (Fig. 1*A*). The "kink" introduced by the imino group of Pro^{1018} may be an essential structural feature, allowing the polypeptide chain to turn back into the plasma membrane to form S6. Our computer modeling studies revealed that leucine introduces local variations in the structure of the loop/turn-helix motif in this position (Fig. 1*C*), increasing conformational flexibility, forming a slightly bigger loop, and slightly unfolding the peptide backbone in the N-terminal part of S6. These changes could relax structural constraints in the mutant channel, with the effect propagated along S6.

Pro^{1018} Is Evolutionarily Conserved. The region between S5 and S6 of "TRPM2-like" channels was recently subdivided into two segments: a highly conserved proximal pore loop and a distal pore loop with very little amino acid similarity (20). Pro^{1018} lies near the end of the distal pore loop and is notably one of the very few conserved residues in this region. Pro^{1018} is conserved among TRPM2 proteins from various species (Fig. 1*D*). The analogous residue is also conserved in some human TRPM subfamily members: TRPM1, TRPM6, TRPM7, and TRPM8 (20) (Fig. S2). Furthermore, the same proline residue is evolutionarily conserved in each of these TRPM channels (Fig. S3). Altogether, these findings suggest that Pro^{1018} may have an important structural and functional role.

P1018L Produces Functional Plasma Membrane Channels that Respond to Oxidative Stress. To assess the potential functional consequences of the Pro-to-Leu substitution experimentally, we created a tetracycline-inducible HEK-293 cell line stably expressing FLAG-tagged human TRPM2 with the Leu^{1018} mutation. We confirmed robust inducible expression of the mutant channel (P1018L) by real-time PCR and Western blot. We further verified presence of the mutation and absence of additional mutations by sequencing (not

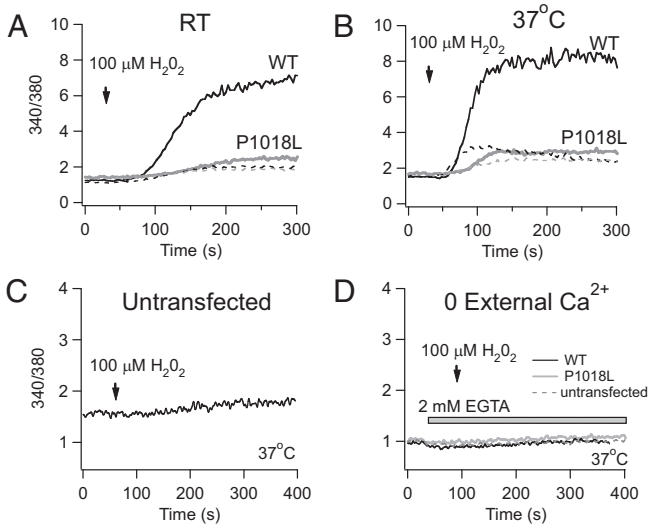

Fig. 2. The Ca^{2+} rise elicited by 100 μM H_2O_2 is attenuated in cells expressing P1018L. Ca^{2+} measurements were performed on Fura-2 loaded HEK-293 cells induced to express WT (black) and P1018L (gray), and in uninduced cells (broken lines) at RT (*A*) and 37°C (*B*). The magnitude of the Ca^{2+} rise in WT was ≈1.2 times greater at 37°C than at RT, and 1.1 times greater at 37 °C than RT for P1018L. The experiments shown in *A* and *B* were done on the same day. (*C*) H_2O_2 (100 μM) did not elicit a similar Ca^{2+} rise in untransfected parental cells, TR-293, which are HEK-293 cells stably expressing the tetracycline repressor (Invitrogen) (*D*) No measurable Ca^{2+} response to 100 μM H_2O_2 is seen in the presence of EGTA.

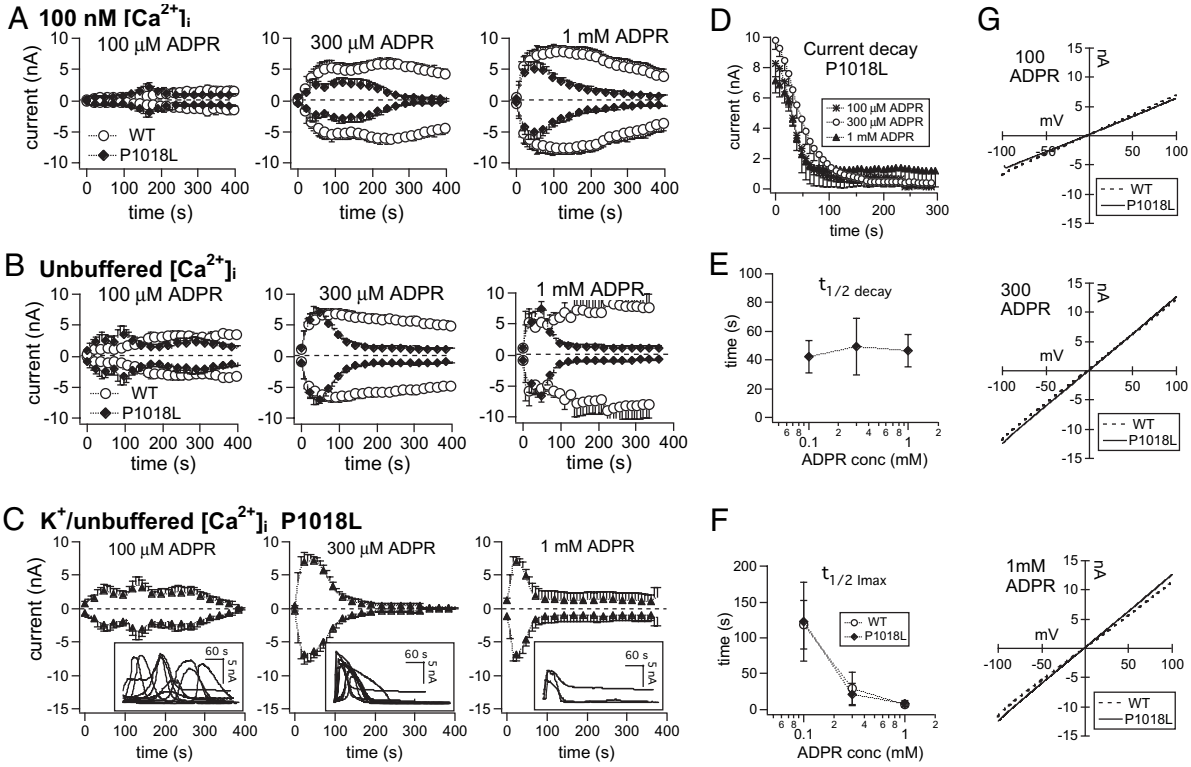

Fig. 3. P1018L inactivation occurs at different ADPR concentrations. (*A–C*) Data traces represent average current development over time (± SEM) measured at −80 and +80 mV in whole-cell patch-clamp experiments. (*A*) Currents elicited by 100 μM ADPR (WT, $n = 18$; P1018L, $n = 13$), 300 μM ADPR (WT, $n = 18$; P1018L, $n = 10$), and 1 mM ADPR (WT, $n = 11$; P1018L, $n = 11$) in the presence of 100 nM $[Ca^{2+}]_i$. (*B*) Unbuffered $[Ca^{2+}]_i$: 100 μM ADPR (WT, $n = 20$; P1018L, $n = 8$), 300 μM ADPR (WT, $n = 14$; P1018L, $n = 16$), and 1 mM ADPR (WT, $n = 10$; P1018L, $n = 6$). The main internal cation (*A* and *B*) is Cs^+. (*C*) Data traces from individual P1018L cells are plotted (insets) along with the average current. The main internal cation is K^+: 100 μM ADPR, $n = 10$; 300 μM ADPR, $n = 11$; 1 mM ADPR, $n = 3$. (*D*) P1018L decay is not influenced by ADPR concentrations. The time course of decay was measured in each cell shown in *C*, then averaged and plotted ± SEM. (*E*) The $t_{1/2\ decay}$ measurements show that P1018L inactivation rate does not change with ADPR concentration. (*F*) WT and P1018L activation rates change similarly in response to increasing ADPR. The $t_{1/2\ Imax}$ provides an approximation of activation rate. (*G*) I/V curves taken at the peak in representative cells (from *B*) show linear WT and P1018L currents reversing close to 0 mV.

shown). We also performed surface biotin-labeling experiments, directly comparing doxycycline-induced P1018L with induced WT TRPM2 in the same expression system (9). As shown in Fig. 1*E*, there is no noticeable difference in surface expression levels, establishing that neither expression nor trafficking is affected in P1018L.

Next, we examined whether P1018L is functional by assessing whether H_2O_2 could elicit $[Ca^{2+}]_i$ rises in Fura 2-loaded cells. We compared H_2O_2-mediated Ca^{2+} influx in induced and uninduced cells (Fig. 2). At room temperature (RT; 23 °C–25 °C), 100 μM H_2O_2 evoked a large $[Ca^{2+}]_i$ rise in WT, but a much more attenuated response in P1018L cells (Fig. 2*A*). Because TRPM2 activation was reported to be temperature sensitive (17, 21), we performed the same experiments on sister cells at 37 °C. Here, the Ca^{2+} response to H_2O_2 was faster and slightly larger in both WT and P1018L cells (Fig. 2*B*). However, the Ca^{2+} rise remained smaller for P1018L compared with WT. In these experiments, this difference stayed relatively constant at approximately fivefold (4.7 at RT and 5.2 at 37 °C). The lower Ca^{2+} rise evoked by H_2O_2 in P1018L cells was consistently observed, even when we used 10 μM, a more physiologically relevant concentration of H_2O_2 (Fig. S4). The same trend was seen at RT and 37 °C, suggesting that the functional effect of the mutation is essentially independent of temperature, at least from RT to 37 °C. In Fig. 2 *A* and *B*, a noticeable $[Ca^{2+}]_i$ rise can be seen in uninduced cells exposed to H_2O_2. This is likely a result of low levels of channel expression occurring despite the tetracycline repressor because it was not evident in untransfected parental cells (Fig. 2*C*). No apparent $[Ca^{2+}]_i$ rise occurred in the absence of extracellular Ca^{2+}, indicating that the Ca^{2+} signals elicited by H_2O_2 in WT and P1018L cells did not come from Ca^{2+} stores (21) (Fig. 2*D*). Overall, our Ca^{2+} experiments show that, whereas P1018L channels can sense and respond to H_2O_2 by allowing Ca^{2+} influx, the resulting Ca^{2+} rise is attenuated. It therefore appears that the Pro-to-Leu substitution renders the channel incapable of mediating Ca^{2+} influx to the same extent as WT.

P1018L Channels Inactivate. To gain a better understanding of how channel function is affected, we conducted whole-cell patch-clamp experiments. Given that ADPR is the most potent activator of TRPM2, and that H_2O_2 effects could arise through increased ADPR production, we first compared WT and P1018L responses to different concentrations of ADPR (100 μM, 300 μM, and 1 mM) added to the pipette solution. The time course of current development in buffered (100 nM $[Ca^{2+}]_i$) and unbuffered $[Ca^{2+}]_i$ conditions with cesium (Cs^+) as the dominant internal cation, are shown in Fig. 3 *A* and *B*, respectively. In the presence of a relatively low dose of ADPR (100 μM) and 100 nM $[Ca^{2+}]_i$, WT and P1018L channels activated slowly, reaching similar average (±SEM) peak amplitudes (WT, 2.3 ± 1.7 nA; P1018L, 3.3 ± 1.9 nA). The same dose of ADPR elicited faster activation and larger currents in unbuffered conditions (WT, 4.3 ± 1.6 nA; P1018L, 6.0 ± 3.5 nA), consistent with reported facilitating effects of internal Ca^{2+} on TRPM2 activation (22, 23). Importantly, WT currents remained sustained over the course of the experiment, whereas P1018L currents inactivated. The latter is not easily seen in the averaged

trace; it gets leveled out by averaging because activation times are highly variable with 100 μM ADPR. For this reason, data traces from individual cells are shown in Fig. 3*C*. Increasing ADPR levels to 300 μM and 1 mM increased peak WT and P1018L current amplitudes and elicited faster activation and more uniform responses among cells. As a result, P1018L inactivation is more accurately reflected by the averaged trace. Potassium (K^+), the physiologically dominant internal cation, elicited similar responses as Cs^+ (Fig. 3*C*).

We analyzed inactivation by measuring the time course of decay starting from the peak until the end of the experiment for each cell, then averaging the results. Current decay over time does not vary with ADPR concentration (Fig. 3*D*). To obtain a more quantitative measure, we determined the time it took for the current to decay to 50% of the peak value, termed $t_{1/2\ decay}$. As shown in Fig. 3*E*, $t_{1/2\ decay}$ remained relatively constant across ADPR concentrations. Finally, we compared WT and P1018L in terms of how their activation rates vary with levels of ADPR. We measured $t_{1/2\ Imax}$, the time required to reach half-maximal current amplitude. As shown in Fig. 3*E*, $t_{1/2\ Imax}$ across ADPR concentrations are very similar for WT and P1018L. Current–voltage (I/V) relationships taken at the peak time point in representative experiments show no difference either: WT and P1018L currents reverse close to 0 mV, as expected for nonselective channels under the ionic conditions used (Fig. 3*G*). Thus, in terms of activation by ADPR, the only difference between WT and P1018L is that the latter inactivates.

P1018L Inactivation Does Not Vary with Internal Ca^{2+}. We sought to determine what could underlie P1018L inactivation. A very important aspect of TRPM2 function is its modulation by extracellular and intracellular Ca^{2+} (22, 23). TRPM2 (WT) reportedly inactivates when $[Ca^{2+}]_i$ decreases to less than 100 nM (22). We wondered if P1018L is similarly affected, perhaps with slightly different sensitivity. In Fig. 4, we show the results of whole-cell patch-clamp experiments on WT and P1018L cells activated by 300 μM ADPR with different $[Ca^{2+}]_i$. We chose to use 300 μM ADPR because, in our hands, this concentration is high enough to provide consistent TRPM2 activation, but not too high as to mask the effects of modulators and other factors of interest such as external and internal Ca^{2+} and Mg^{2+}. P1018L inactivated at all concentrations of $[Ca^{2+}]_i$ tested, from 10 nM to 1 μM (Fig. 3 *A–C*), and when left unbuffered (not shown). A certain degree of WT inactivation occurred in the presence of low $[Ca^{2+}]_i$ (at 10 and 50 nM), but not in every cell, and not to the same extent as P1018L, which generally disappears completely. I/V relationships, measured at the peak and plotted, show WT and P1018L currents reversing close to 0 mV in the presence of very low (10 nM) and very high (1 μM) internal Ca^{2+}. Peak WT and P1018L current amplitudes did not vary as $[Ca^{2+}]_i$ changed (Fig. 4*D*, *Left*). Similar to ADPR, the most notable effect of increasing $[Ca^{2+}]_i$ is to speed up WT and P1018L channel activation (Fig. 4*D*, *Right*). The time course of current decay remained similar in different $[Ca^{2+}]_i$ concentrations (Fig. 4*E*), suggesting that the mechanistic basis of P1018L inactivation stems from the Pro-to-Leu substitution, unlike WT inactivation, which occurs in only very low $[Ca^{2+}]_i$ (22).

P1018L Does Not Inactivate at Very Low External Ca^{2+}. The extracellular region spanning the pore loop to the outer half of S6, where Pro^{1018} is, has been implicated in C-type inactivation of *Shaker* K^+ channels, inactivation of voltage-gated Ca^{2+} channels, and acid-induced inactivation of TRPM5 (24–27). We examined if varying external Ca^{2+} levels could affect P1018L function. The results are dramatic (Fig. 5*A*). Inactivation slowed down as external Ca^{2+} is lowered, completely disappearing when Ca^{2+} was reduced to 30 μM. No P1018L activation was observed when Ca^{2+} was omitted from the bath. I/V relationships did not vary as external Ca^{2+} was changed (Fig. 5*B*). The time course of decay at different external Ca^{2+} concentrations is shown in Fig. 5*C* (*Left*), except for 30 μM

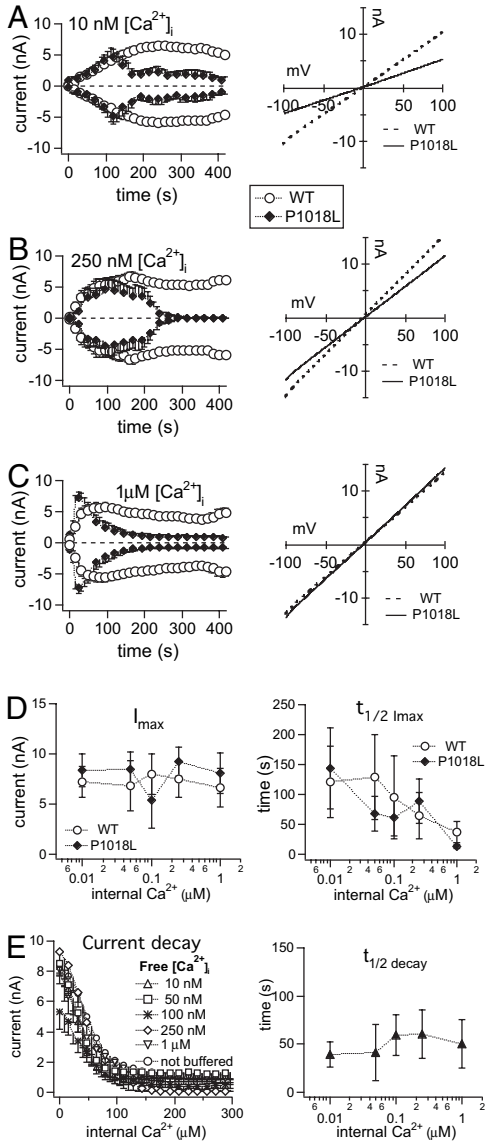

Fig. 4. P1018L inactivation is not affected by changes in $[Ca^{2+}]_i$. (*A–C*) Time course of WT and P1018L current development elicited by 300 μM ADPR with different concentrations of $[Ca^{2+}]_i$. Shown are average currents (±SEM) measured at −80 and +80 mV. I/V curves, taken at the peak in representative cells and plotted (*Right*), show P1018L (solid lines) and WT (broken lines) currents reversing close to 0 mV. P1018L inactivated at all $[Ca^{2+}]_i$, e.g., 10 nM (WT, $n = 17$; P1018L, $n = 9$), 250 nM (WT, $n = 10$; P1018L, $n = 7$), and 1 μM (WT, $n = 13$; P1018L, $n = 8$). (*D*) Dose–response plots of peak current amplitudes (I_{max}) and activation rates ($t_{1/2\ Imax}$) at different $[Ca^{2+}]_i$. I_{max} stayed relatively constant across $[Ca^{2+}]_i$ concentrations for both WT and P1018L (*Left*). Activation was faster as $[Ca^{2+}]_i$ levels increased (*Right*). The I_{max} and $t_{1/2\ Imax}$ are not significantly different in WT and P1018L. (*E*) P1018L decay is not influenced by $[Ca^{2+}]_i$. Averaged current decay traces ± SEM (*Left*) and $t_{1/2\ decay}$ (*Right*). The number of P1018L cells averaged for the $[Ca^{2+}]_i$ concentrations not previously listed are as follows: 50 nM, $n = 10$; 100 nM, $n = 10$; not buffered, $n = 16$.

Ca^{2+}, with which no decay occurred. We also evaluated $t_{1/2\ decay}$, which decreased as external Ca^{2+} levels increased (Fig. 5*C*, *Right*). No $t_{1/2\ decay}$ values could be measured when external Ca^{2+} was lower than 300 μM because currents did not decay to half of the peak amplitude in those conditions. Activation occurred faster as external Ca^{2+} levels increased (Fig. 5*D*, *Left*). The average peak current amplitude also increased, but only when external Ca^{2+} is present at 300 μM and higher (Fig. 5*D*, *Right*) suggesting that, at these concentrations, Ca^{2+} permeating TRPM2 could accumulate inter-

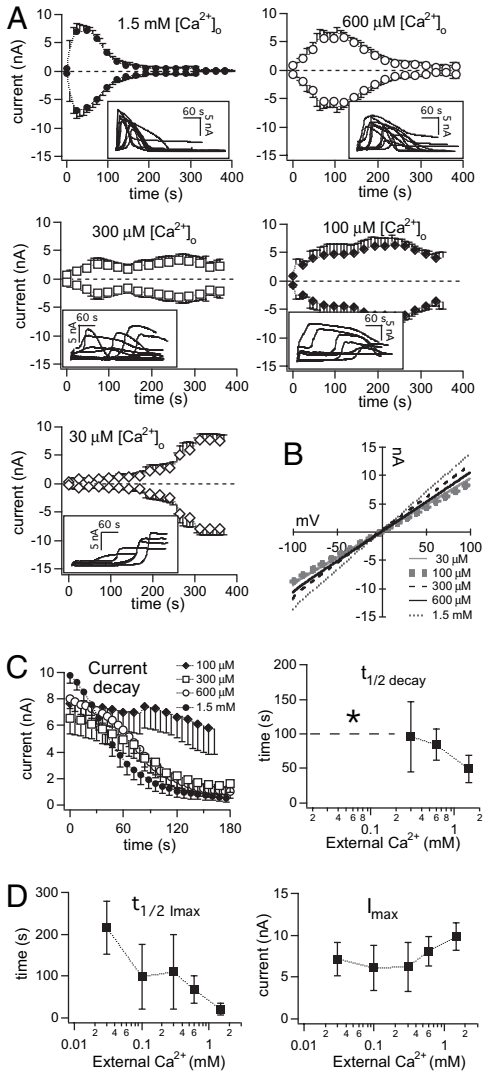

Fig. 5. Changes in external Ca^{2+} concentrations, $[Ca^{2+}]_o$, affect P1018L inactivation. (*A*) Time course of P1018L current development elicited by 300 μM ADPR in the presence of decreasing $[Ca^{2+}]_o$ and unbuffered $[Ca^{2+}]_i$. Shown are average currents (±SEM) measured at −80 and +80 mV, and currents measured at +80 mV from individual cells (insets). Data traces for 1.5 mM external Ca^{2+} are from Fig. 3*C*, *Middle*. The number of cells averaged for each $[Ca^{2+}]_o$: 600 μM, $n = 10$; 300 μM, $n = 10$; 100 μM, $n = 8$; 30 μM, $n = 5$. (*B*) I/V curves taken at the peak in representative cells. (*C*) Average time course of decay ± SEM (*Left*) and $t_{1/2\ decay}$ (*Right*) in different $[Ca^{2+}]_o$. P1018L did not inactivate at 30 μM $[Ca^{2+}]_o$. The $t_{1/2\ decay}$ was not measurable for 30 μM and 100 μM $[Ca^{2+}]_o$. (*D*) P1018L activated faster as $[Ca^{2+}]_o$ increased (*Left*). The I_{Max} also increased as $[Ca^{2+}]_o$ increased from 300 μM to 600 μM, up to 1.5 mM (*Right*).

nally, reaching levels that facilitate the activation of more TRPM2 channels.

P1018L Inactivation Is Not Affected by Mg^{2+} or Higher Temperature. Next, we examined whether external or internal Mg^{2+} plays any role in P1018L inactivation. Withholding Mg^{2+} from the external or internal solutions, or from both, did not have any effect on inactivation (Fig. S5 *A–C*). The time course of decay remained similar (Fig. S5*D*). Peak current amplitude was not affected either (data not shown), but P1018L activation becomes significantly delayed when Mg^{2+} is absent from both external and internal solutions (Fig. S5*E*). This delay was not observed in WT, in which $t_{1/2\ Imax}$ measurements were 24.3 ± 11.6 s (no external and internal Mg^{2+}) and 29.2 ± 22.9 s (with external and internal Mg^{2+}). Finally, we checked if temperature has any effect on P1018L inactivation. Whole-cell patch-clamp data using buffered and unbuffered Ca^{2+} conditions show that inactivation persists at 37 °C (Fig. S6 *A* and *B*). There was no significant difference in inactivation kinetics between experiments performed at RT or 37 °C.

Thus, except for external Ca^{2+}, P1018L inactivation is relatively immune to changes in the concentrations of ADPR, internal Ca^{2+}, internal and external Mg^{2+}, and even temperature.

L-BMAA Slightly Attenuates H_2O_2-Induced Ca^{2+} Increases in WT and P1018L Cells. We also examined the effects of the putative neurotoxin L-BMAA on P1018L channels. We found that 1 mM L-BMAA causes slight reduction of WT and P1018L currents in whole-cell patch-clamp experiments (Fig. S7*A*). Consistent with this, we also detected slight attenuation of the Ca^{2+} increase elicited by H_2O_2 in WT and P1018L cells pre-exposed to L-BMAA (Fig. S7*B*).

Discussion

We have described a heterozygous variant of TRPM2, *TRPM2*^{P1018L}, in which Pro^{1018} is changed to Leu^{1018}. Computer modeling studies predict that Leu^{1018} increases conformational flexibility at the N-terminal end of S6. Using Fura-2 to report $[Ca^{2+}]_i$ changes and whole-cell patch-clamp experiments to study channel function, we have shown that P1018L forms functional channels that activate in response to H_2O_2 and ADPR. However, in the presence of physiological concentrations of extracellular Ca^{2+}, P1018L channels inactivate quickly and are thus unable to allow sustained ion influx. In intact cells, this is manifested as an attenuated Ca^{2+} rise in response to H_2O_2. Exposure to L-BMAA slightly reduces both WT and P1018L currents, further aggravating the deficient Ca^{2+} response in P1018L cells. Defective Ca^{2+} handling is implicated in many diseases, including neurodegeneration. Of particular interest is a recent report that described another Pro-to-Leu substitution, this time in CalHM1, a putative Ca^{2+}-permeable channel (28). *CalHM1*^{P86L} increases risk for Alzheimer's disease. In functional studies, cells expressing $CalHM1^{P86L}$ proteins exhibited attenuated Ca^{2+} permeability, reduced cytosolic Ca^{2+} levels, and increased amyloid β deposition. The similarity in the effects of $CalHM1^{P86L}$ and $TRPM2^{P1018L}$ suggests that attenuation of intracellular Ca^{2+} rises and its effects on downstream signaling pathways may contribute to the pathophysiological mechanism in neurodegenerative diseases.

What Mechanism Underlies P1018L Inactivation? P1018L inactivation becomes more rapid as external Ca^{2+} levels increase, suggesting that conformational changes leading to inactivation are favored as more Ca^{2+} ions occupy binding sites in the pore domain of the mutant, but not WT, TRPM2. Pro^{1018} is located in the region that forms the junction between the distal end of the pore and the beginning of S6, 35 to 37 residues away from Q981 and P983, both implicated in the broad cation selectivity of TRPM2 (20). Our modeling studies predict that replacement of Pro^{1018} with Leu causes the formation of a slightly bigger loop in this region, and slight unfolding the peptide backbone in the N-terminal end of S6. These changes are predicted to relax structural constraints, increasing conformational flexibility that could destabilize the outer pore domain. Our studies suggest that the conformational changes leading to occlusion of the pore are favored when more Ca^{2+} ions are bound to binding sites in the pore domain of P1018L channel. By contrast, Pro^{1018} maintains the required structural rigidity in this region (see Fig. S8 for a schematic illustration of this model). This very preliminary hypothesis is patterned after the current model for slow C-type inactivation of K^+ channels, which also involves residues in this region (24, 25). We do not yet know if the relative permeability to Ca^{2+} and Na^+ are affected in the mutant. These, and studies designed to elucidate the mechanism of inactivation

NEUROSCIENCE

further, are among future studies planned to functionally characterize this disease-relevant mutant channel.

The physiological consequences of the P1018L phenotype will ultimately depend on the cellular processes that lie downstream of TRPM2-mediated Ca^{2+} influx in each cell type. TRPM2 is highly expressed in the brain, in both microglia and neuronal cells, but its biological role in these cells still needs to be understood. Studies suggest that Ca^{2+} influx via TRPM2 is necessary for microglia and other phagocytes to mount effective inflammatory and clearance responses (10, 29). An important advance in our understanding of the biological role of TRPM2 is provided by a recent study on *TRPM2*-KO mice (30). Although indistinguishable from WT mice in terms of gross phenotypic characteristics, the H_2O_2-activated signaling cascade involved in the production of macrophage inflammatory protein-2 cytokine is impaired in monocytes from *TRPM2*-KO mice. H_2O_2-evoked Ca^{2+} influx was almost abolished. It is possible that the effect of P1018L will be similar to *TRPM2*-KO, but we must keep in mind that H_2O_2 elicits a Ca^{2+} rise in P1018L-expressing cells, albeit much less than WT. Because signaling cascades that control cellular processes are affected by the amplitude, speed, duration, and spatio-temporal patterns of intracellular Ca^{2+} variations (31), it is possible that the functional effects of a low Ca^{2+} rise via P1018L will be different from an almost absent Ca^{2+} rise in *TRPM2*-KO. Only studies performed in P1018L transgenic mice will answer this question.

Lynch *et al.* (32) recently proposed a novel gene/environment interaction model in which the combined effects of eight risk factors for ALS-G/PD-G (among them $TRPM7^{T1482I}$ and mitochondrial DNA mutations) provided a statistically significant predisposition to these disorders. It would be interesting to include $TRPM2^{P1018L}$ in that analysis. Altogether, 6 of 13 cases of ALS-G and three of nine cases of PD-G had either the $TRPM2^{P1018L}$ or $TRPM7^{T1482I}$ variant, and one PD-G case had both. There remain 7 of 13 ALS-G cases and five of nine PD-G cases in our sample set in which neither variant was found, highlighting the complex, multifactorial nature of the etiology of these disorders. Importantly, we found only heterozygous forms of $TRPM2^{P1018L}$ or $TRPM7^{T1482I}$. By necessity, our initial functional studies of the variants were performed on expressed mutant channels compared with their WT counterparts. Planned future studies include investigations of the interaction between WT and mutants, as well as analysis of dominant or codominant effects in heterozygotes.

Our approach of using the environmental risk factors in ALS-G and PD-G to identify functional candidate susceptibility genes has resulted in the identification of *TRPM2* and *TRPM7* variants in these disorders. These are significant contributions to ongoing research efforts aimed at understanding how gene/environment interactions contribute to the pathogenesis of ALS-G and PD-G.

Materials and Methods

Genotyping. Primer sequences were designed based on the published human sequence for *TRPM2* (NC_000021.7) and available on request. Sequences were aligned against National Center for Biotechnology Information *TRPM2* genomic and mRNA reference sequences (NC_000021.7 and NM_003307, respectively). Detailed description of all methods and pertinent references are provided in *SI Text*

Computer Modeling and Structural Prediction of S6 in TRPM2 and $TRPM2^{P1018L}$. We used the HHpred remote homology-detection server, selected a K^+ voltage-gated channel subfamily A member (Protein Data Bank code 2a79_B) as a good candidate structural template for the S6 of TRPM2, and used this structure to build the comparative models.

Fura-2 Ca^{2+} Experiments. Cytosolic $[Ca^{2+}]$ was monitored in a cuvette-based assay by detecting changes in Fura-2 fluorescence using the QM-6/2003 fluorometer (Photon Technology International).

Electrophysiology. The cells were induced with doxycycline for 16 to 22 h. Patch-clamp experiments were performed at RT, unless otherwise specified, in the tight-seal, whole-cell configuration (7).

ACKNOWLEDGMENTS. We thank D.S. Haymer, I.M. Cooke, and M.D. Rayner for critical reading of the manuscript and thoughtful comments. This work was supported by National Institutes of Health (NIH) grant S11 NS043462 (to M.C.H.), the Cades Foundation (M.C.H), a junior investigator award from the Sandler Program in Asthma Research (A.L.P), and NIH grant K08AI060926 (to C.S.).

1. Garruto RM (2006) A Commentary on neuronal degeneration and cell death in Guam ALS and PD: an evolutionary process of understanding. *Curr Alzheimer Res* 3:397–401.
2. Yase Y (1972) The pathogenesis of amyotrophic lateral sclerosis. *Lancet* 2:292–296.
3. Spencer PS, *et al.* (1987) Guam amyotrophic lateral sclerosis-parkinsonism-dementia linked to a plant excitant neurotoxin. *Science* 237:517–522.
4. Yanagihara R, *et al.* (1984) Calcium and vitamin D metabolism in Guamanian Chamorros with amyotrophic lateral sclerosis and parkinsonism-dementia. *Ann Neurol* 15:42–48.
5. Oyanagi K, *et al.* (2006) Magnesium deficiency over generations in rats with special references to the pathogenesis of the Parkinsonism-dementia complex and amyotrophic lateral sclerosis of Guam. *Neuropathology* 26:115–128.
6. Hermosura MC, Garruto RM (2007) TRPM7 and TRPM2-Candidate susceptibility genes for Western Pacific ALS and PD? *Biochim Biophys Acta* 1772:822–835.
7. Hermosura MC, *et al.* (2005) A TRPM7 variant shows altered sensitivity to magnesium that may contribute to the pathogenesis of two Guamanian neurodegenerative disorders. *Proc Natl Acad Sci USA* 102:11510–11515.
8. Sano Y, *et al.* (2001) Immunocyte Ca^{2+} influx system mediated by LTRPC2. *Science* 293:1327–1330.
9. Perraud AL, *et al.* (2001) ADP-ribose gating of the calcium-permeable LTRPC2 channel revealed by Nudix motif homology. *Nature* 411:595–599.
10. Kraft R, *et al.* (2004) Hydrogen peroxide and ADP-ribose induce TRPM2-mediated calcium influx and cation currents in microglia. *Am J Physiol Cell Physiol* 286:C129- C137.
11. Kaneko S, *et al.* (2006) A critical role of TRPM2 in neuronal cell death by hydrogen peroxide. *J Pharmacol Sci* 101:166–176.
12. Nilius B, Owsianik G, Voets T, Peters JA (2007) Transient Receptor Potential cation channels in disease. *Physiol Rev* 87:165–217.
13. Clapham DE (2007) Snapshot: mammalian TRP channels. *Cell* 129:220.
14. Kuhn FJ, Luckhoff A (2004) Sites of the NUDT9-H domain critical for ADP-ribose activation of the cation channel TRPM2. *J Biol Chem* 279:46431–46437.
15. Heiner I, *et al.* (2006) Endogenous ADP-ribose enables calcium-regulated cation currents through TRPM2 channels in neutrophil granulocytes. *Biochem J* 398:225–232.
16. Hara Y, *et al.* (2002) LTRPC2 Ca^{2+}-permeable channel activated by changes in redox status confers susceptibility to cell death. *Mol Cell* 9:163–173.
17. Togashi K, *et al.* (2006) TRPM2 activation by cyclic ADP-ribose at body temperature is involved in insulin secretion. *EMBO J* 25:1804–1815.
18. Perraud AL, *et al.* (2005) Accumulation of free ADP-ribose from mitochondria mediates oxidative stress-induced gating of TRPM2 cation channels. *J Biol Chem* 280:6138–6148.
19. Winn M, *et al.* (2005) A mutation in the TRPC6 cation channel causes familial focal segmental glomerulosclerosis. *Science* 308:1801–1804.
20. Mederos y Schnitzler M, Waring J, Gudermann T, Chubanov V (2008) Evolutionary determinants of divergent calcium selectivity of TRPM channels. *FASEB J* 22:1540–1551.
21. Wilkinson JA, Scragg JL, Boyle JP, Nilius B, Peers C (2008) H_20_2-stimulated Ca^{2+} influx via TRPM2 is not the sole determinant of subsequent cell death. *Pflugers Arch* 455:1141–1151.
22. Starkus J, Beck A, Fleig A, Penner R (2007) Regulation of TRPM2 by extra- and intracellular calcium. *J Gen Physiol* 130:427–440.
23. McHugh D, Flemming R, Xu SZ, Perraud AL, Beech DJ (2003) Critical intracellular Ca^{2+} dependence of transient receptor potential melastatin 2 (TRPM2) cation channel activation. *J Biol Chem* 278:11002–11006.
24. Hoshi T, Zagotta WN, Aldrich RW (1991) Two types of inactivation in Shaker K^+ channels: effects of alterations in the carboxy-terminal region. *Neuron* 7:547–556.
25. Liu Y, Jurman ME, Yellen G (1996) Dynamic rearrangement of the outer mouth of a K^+ channel during gating. *Neuron* 16:859–867.
26. Zhang JF, Ellinor PT, Aldrich, RW Tsien RW (1994) Molecular determinants of voltage-dependent inactivation in calcium channels. *Nature* 372:97–100.
27. Liu D, Zhang Z, Liman ER (2005) Extracellular acid block and acid-enhanced inactivation of the Ca^{2+}-activated cation channel TRPM5 involve residues in the S3–S4 and S5–S6 extracellular domains. *J Biol Chem* 280:20691–20699.
28. Dreses-Werringloer U, *et al.* (2008) A Polymorphism in CALHM1 influences Ca^{2+} homeostasis, Aß levels, and Alzheimer's disease risk. *Cell* 133:1149–1161.
29. Partida-Sanchez SA, *et al.* (2007) Chemotaxis of mouse bone marrow neutrophils and dendritic cells is controlled by ADP-ribose, the major product generated by the CD38 enzyme reaction. *J Immunol* 179:7827–7839.
30. Yamamoto S, *et al.* (2008) TRPM2-mediated Ca^{2+} influx induces chemokine production in monocytes that aggravates inflammatory neutrophil infiltration. *Nat Med* 14:738–747.
31. Berridge MJ, Lipp P, Bootman MD (2000) The versatility and universality of calcium signalling. *Nat Rev Mol Cell Biol* 1:11–21.
32. Lynch D, *et al.* (2008) The contribution of mitochondrial dysfunction to a gene-environment model of Guamanian ALS and PD. *Mitochondrion* 8:109–116.